A 3-D Printed Halbach-Cylinder Motor With Self-Position Sensing for Precision Motions

Yuan Wei, Vu Huy Nguyen, *Member, IEEE*, and Won-Jong Kim, *Senior Member, IEEE*

***Abstract*—This article presents the design and control of a new Halbach-array-based two-phase motor (HTM) with a 3-D printed coil mount and magnet housing for precision motion control applications. The motor is based on a two-pole Halbach cylinder that generates a uniform magnetic field within its inner diameter. Each pole has 10 magnet segments. This uniform field simplifies the Lorentz force calculation based on the volume integration. In addition, it allows for the real-time measurement of the rotor position based on Hall-effect sensors. Compared with conventional stepper motors and iron-core dc motors, this motor design can produce a continuous torque and precise positioning at any angular position without a cogging torque. In this article, the design of the motor together with its dynamics and control are presented. The design uses only one type of square-cross-section magnets that are readily available, making it easy to scale the design to a variety of sizes and torque capabilities. The 3-D printed stator and rotor housings allow for the motor to be constructed at a low cost in a short time. With a total magnet volume of only 30.7 cm^3, a total effective coil volume of only 10.4 cm^3, and a maximum current of 4 A, the maximum torque generated is 0.044 N·m. Experimental results with closed-loop control on a simple empirically identified plant model are provided to validate the magnetic design of the motor. The feedback signals are from two Hall-effect sensors connected to a microcontroller, offering a theoretical angular resolution of 0.16°. A minimum step size of 0.32° is demonstrated in positioning with closed-loop control. The motor has the capacity to track the commanded motion and speed with an error less than 0.64°.**

***Index Terms*—Continuous torque, Halbach cylinder motor, Halbach magnet array, Lorentz force, permanent-magnet (PM) machine.**

I. Introduction

THERE are particular applications where the need for a low-cost electric motor having a highly precise positioning capability with no Eddy-current loss, cogging force, and backlash is critical. The lidar- or radar-position-control motors for autonomous vehicles are such an example [1]. For this application, precise positioning is required to avoid the distortions of the constructed images [2], and zero Eddy-current loss is needed to enhance the power efficiency and to avoid damages due to excessive heat generated during continuous operations. In addition, the mechanical transmissions should be excluded to avoid the added inertia, friction, and backlash. In this context, a Halbach-cylinder motor design stands out as one of the most suitable motor structures for the above-mentioned applications. This article presents the design and validation of a Halbach-cylinder rotary motor, which is a brushless, ironless motor with the planar Lorentz coils generating a continuous torque at any angular position, and the 3-D printable stator and rotor housings for the ease of fabrication. Fig. 1 is a photograph of the entire experimental setup of the motor and the control hardware. Fig. 2 shows a cross-sectional view of the motor, which is an external-rotor design.

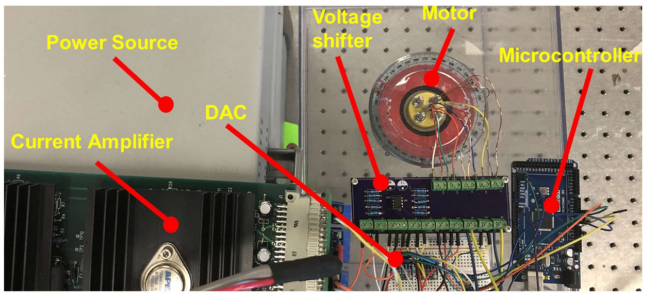

Fig. 1. Photograph of the experimental setup of the motor and the hardware.

A Halbach magnet array, as first introduced in [3] and later used in high-power-density rotary and linear motors designed for precision applications [4]–[11], is a structure formed by multiple permanent magnets (PMs) ideally with the same shape and with the magnetization directions discretely rotated by a fixed angular step along a certain dimension of the structure. This configuration helps strengthen the magnetic field on one side and cancel the field on the other side of the magnet array. A Halbach cylinder is constructed by magnet pieces arranged around the circumference of a circle [4], [6], [8], [9]. Depending on the magnetization's rotational direction of the PMs, the magnetic field can be focused on the outer or inner side of the hollow cylinder. In the case of focusing the field in the interior of the cylinder, as in our case illustrated in Fig. 2, theoretically,

Manuscript received December 26, 2020; revised April 5, 2021; accepted May 7, 2021. Date of publication June 8, 2021; date of current version June 16, 2022. Recommended by Technical Editor W. Kim and Senior Editor X. Tan. *(Corresponding author: Vu Huy Nguyen.)*

Yuan Wei and Won-Jong Kim are with the Department of Mechanical Engineering at Texas A&M University, College Station, TX 77840 USA (e-mail: weiyuan1996@tamu.edu; wjkim@tamu.edu).

Vu Huy Nguyen is with the Lawrence Berkeley National Laboratory, Berkeley, CA 94720 USA (e-mail: vu_nguyen@ieee.org).

Color versions of one or more figures in this article are available at https://doi.org/10.1109/TMECH.2021.3087523.

Digital Object Identifier 10.1109/TMECH.2021.3087523

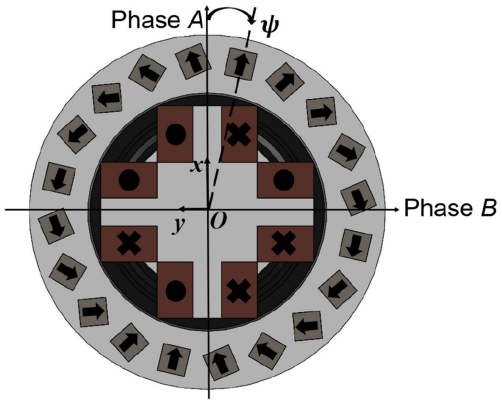

Fig. 2. Cross-sectional view of our Halbach-cylinder motor.

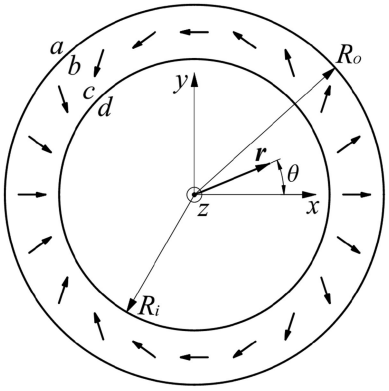

Fig. 3. Illustration of the general Halbach cylinder.

a uniform field can be formed within the inner radius of the Halbach cylinder if it has one spatial period (or two poles) of the Habach array. Practically, the field can be non-uniform due to the segmentation of the cylinder into the commercially available discrete magnet pieces that enables the fabrication of the structure and errors in the magnets' local magnetization directions and remanence [12]–[14]. For a Lorentz-force motor where the outer rotor is a Halbach cylinder, the torque model's linearity directly results from the field's uniformity. Therefore, it is of critical necessity to come up with a Halbach-cylinder motor design with an optimally uniform field while offering the advantages of the low cost, ease of fabrication and control, and scalability of the structure.

A number of Halbach-cylinder motors have been previously constructed [4], [6], [8]. However, they were iron-cored motors that unavoidably exhibited Eddy-current loss and cogging torques due to saliency, which we want to avoid. In [9], an ironless actuator with a Lorentz coil and a Halbach cylinder was presented. However, this motor could only work in a limited angular range with nonuniform torque and could not continuously rotate to make a full revolution. Here we present a Lorentz-force Halbach cylinder motor design with the key contributions of:

1) using rectangular coils and square cross-sectional magnets to allow for low-cost and scalable manufacturing of the motors;
2) employing two-phase currents to allow for the continuous positioning of the rotor at any angular position;
3) using the Halbach cylinder's magnetic field for the real-time angular-position measurement of the rotor.

In addition, we provide an empirically derived system model on which a simple proportional-integral (PI) controller is designed for the motor to perform precision positioning and tracking.

The rest of this article is organized as follows. Section II of this article presents the magnetic, mechanical, and electronic hardware design for the position sensing and control of the Halbach-array-based two-phase motor (HTM). Section III discusses the dynamics and control, including the identification of the motor's system model, and provides the closed-loop control experimental results. Finally, Section IV concludes this article.

II. Magnetic, Mechanical, and Hardware Design

A. Magnetic Field Solution for the Halbach Cylinder

An ideal Halbach magnet cylinder is a hollow and infinitely long cylindrical PM structure whose magnetization direction continuously rotate in only one way (either counterclockwise or clockwise) along the cylinder's azimuthal direction with a fixed angular period [15]–[17]. In case of focusing the field into its interior, such an ideal Halbach cylinder with two poles generates a uniform magnetic field, and its flux density depends on the cylinder's geometry and the remanence of the PM material. Fig. 3 illustrates a Halbach cylinder with R_o and R_i being its outer and inner radii. The arrows in the cylindrical magnet volume between R_i and R_o represent the local magnetization magnitudes and directions.

With the variation of the magnetization directions as in Fig. 3, the resultant magnetic field of the entire cylinder is focused into the cylinder's inner space with $r < R_i$. The derivation of the field solution is started by solving the Poison equation (1) for the vector potential $\boldsymbol{A}$ using the magnetization $\boldsymbol{M}$ and the boundaries of a, b, c, and d as in Fig. 3

$$\nabla^2 \boldsymbol{A} = -\mu_0 \nabla \times \boldsymbol{M}. \tag{1}$$

The magnetization $\boldsymbol{M}$ of a periodic magnet placement around the cylinder's circumference can be expressed as a Fourier series expansion

$$\begin{aligned} \boldsymbol{M} &= M_r \, \boldsymbol{i}_r + M_\theta \boldsymbol{i}_\theta \\ &= \sum_{n=1}^{\infty} M_{rn} \cos(n\theta) \, \boldsymbol{i}_r + M_{\theta n} \sin(n\theta) \, \boldsymbol{i}_\theta. \end{aligned} \tag{2}$$

Here, M_{rn} and $M_{\theta n}$ are nth Fourier harmonics of its r- and θ-components, respectively. In our case, we have $M_{rn} = M_{\theta n}$ [18]. With (2), (1) becomes

$$\nabla^2 \boldsymbol{A}_n = -\frac{\mu_0}{r} \left(M_{rn} + n M_{\theta n} \right) \sin(n\theta) \, \boldsymbol{i}_z. \tag{3}$$

Here, $\boldsymbol{A}_n$ is the nth-order Fourier harmonics of the vector potential $\boldsymbol{A}$. With $\boldsymbol{M}$ only in the r–θ plane, $\boldsymbol{A}_n$ is written as

$$\boldsymbol{A}_n = A_{zn}(r) \sin(n\theta) \, \boldsymbol{i}_z. \tag{4}$$

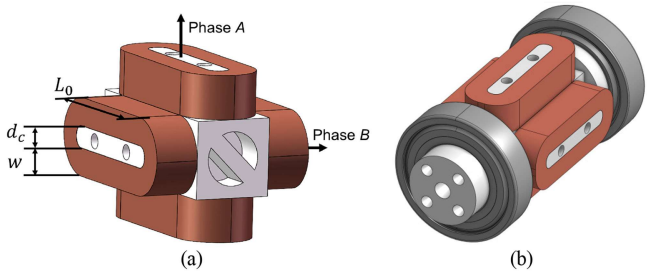

Fig. 4. 3-D rendering of (a) the motor's inner stator with four coils wrapping around the 3D printed stator housing and (b) the stator with the two bearings.

Substituting (4) to (3), yielding

$$\frac{\partial^2 A_{zn}}{\partial r^2}+\frac{1}{r}\cdot\frac{\partial A_{zn}}{\partial r}-\frac{n^2}{r^2}A_{zn}=-\frac{\mu_0}{r}\left(M_{rn}+nM_{\theta n}\right). \quad (5)$$

The homogeneous solution to (5) is provided in (6) [18].

$$A_{zn\_h}(r)=C_{n1}\,r^n+C_{n2}r^{-n}. \quad (6)$$

Here C_{n1} and C_{n2} are the constants to be determined by the boundary conditions. In this article, we present the derivation of the field solution corresponding to the fundamental harmonics and compare the result with the measured magnetic field for our Halbach cylinder.

With $B_{re}=\mu_0(M_{r1}+M_{\theta 1})/2$, a particular solution of (5) for the fundamental harmonics is given as [18]

$$A_{z1\_p}(r)=-B_{re}r\ln(r). \quad (7)$$

The general solution to (5) for the fundamental harmonics is

$$A_{z1}(r)=C_{11}r+C_{12}r^{-1}-B_{re}r\ln(r). \quad (8)$$

At the boundaries of b and c as in Fig. 4, we have $A_{z1}=A_{z1}^b$ and $A_{z1}=A_{z1}^c$, respectively. Substituting this into (8) and solve for C_{11} and C_{12}, we obtain

$$\mathrm{C}_{11}=\frac{1}{R_o^2-R_i^2}\times\left\{A_{z1}^bR_o-A_{z1}^cR_i+B_{re}\left[R_o^2\ln(R_o)-R_i^2\ln(R_i)\right]\right\} \quad (9)$$

$$\mathrm{C}_{12}=A_{z1}^cR_i+B_rR_i^2\ln(R_i)-\frac{R_i^2}{R_o^2-R_i^2}\times\left\{A_{z1}^bR_o-A_{z1}^cR_i+B_{re}\left[R_o^2\ln(R_o)-R_i^2\ln(R_i)\right]\right\}. \quad (10)$$

In the cylindrical coordinate, $\boldsymbol{B}=\nabla\times\boldsymbol{A}$ is expressed as

$$\boldsymbol{B}=\frac{1}{r}\begin{vmatrix}\boldsymbol{i}_r & r\boldsymbol{i}_\theta & \boldsymbol{i}_z\\ \frac{\partial}{\partial r} & \frac{\partial}{\partial\theta} & 0\\ 0 & 0 & A_{z1}\sin(\theta)\end{vmatrix}=\frac{A_{z1}}{r}\cos(\theta)\,\boldsymbol{i}_r-\frac{\partial A_{z1}}{\partial r}\sin(\theta)\,\boldsymbol{i}_\theta. \quad (11)$$

Considering only the fundamental harmonics, $\boldsymbol{B}$ is expressed as

$$\boldsymbol{B}_1=B_{r1}\cos(\theta)\,\boldsymbol{i}_r+B_{\theta 1}\sin(\theta)\,\boldsymbol{i}_\theta \quad (12)$$

where $B_{\theta 1}=-\frac{\partial A_{z1}}{\partial r}$. With this, the transfer relations between $B_{\theta 1}$ and A_{z1} at the boundaries b and c are as [18], [19]

$$\begin{bmatrix}B_{\theta 1}^b\\ B_{\theta 1}^c\end{bmatrix}=\begin{bmatrix}K_{11} & K_{12}\\ K_{21} & K_{22}\end{bmatrix}\begin{bmatrix}A_{z1}^b\\ A_{z1}^c\end{bmatrix}+\begin{bmatrix}L_b\\ L_c\end{bmatrix}B_{re} \quad (13)$$

$$K_{11}=\frac{R_i^2+R_o^2}{R_o\left(R_i^2-R_o^2\right)},K_{12}=\frac{2R_i}{R_o^2-R_i^2},K_{21}=\frac{2R_o}{R_i^2-R_o^2},$$
$$K_{22}=\frac{R_i^2+R_o^2}{R_i\left(R_o^2-R_i^2\right)},L_b=1+\frac{2R_i^2\left[\ln(R_i)-\ln(R_o)\right]}{R_o^2-R_i^2},$$
$$L_c=1+\frac{2R_o^2\left[\ln(R_i)-\ln(R_o)\right]}{R_o^2-R_i^2}. \quad (14)$$

Utilizing the transfer relations [19], the relations between the magnetic flux density $B_{\theta 1}$ and the magnetic vector potential A_{z1} at a and d are found as follows [18]:

$$B_{\theta 1}^a=\frac{1}{R_o}A_{z1}^a,B_{\theta 1}^d=-\frac{1}{R_i}A_{z1}^d. \quad (15)$$

The vector potential is continuous at the boundaries, therefore

$$A_{z1}^a=A_{z1}^b,A_{z1}^c=A_{z1}^d. \quad (16)$$

The jumps in the magnetic flux densities at the boundaries *a*-*b* and *c*-*d* are represented as

$$-B_{\theta 1}^a+B_{\theta 1}^b=B_{re} \quad (17)$$

$$-B_{\theta 1}^c+B_{\theta 1}^d=B_{re}. \quad (18)$$

Here, B_{re} is defined in (7) and also the remanence of the magnet material of the cylinder.

From (13) and (15)–(18), a set of eight equations with eight variables, which are A_{z1} and $B_{\theta 1}$ at a, b, c, and d, is formed. Solving this set of equation, we get the following result:

$$\left[A_{z1}^a\ A_{z1}^b\ A_{z1}^c\ A_{z1}^d\ B_{\theta 1}^a\ B_{\theta 1}^b\ B_{\theta 1}^c\ B_{\theta 1}^d\right]=\left[0\ \ 0\ \ (B_{re}R_i\ln\rho)\ \ (B_{re}R_i\ln\rho)\ \ 0\ \ B_{re}\ B_{re}(1-\ln\rho)\ \ (-B_{re}\ln\rho)\right]. \quad (19)$$

Here, $\rho=R_o/R_i$. At (r_0,θ_0) in the cylinder, where $r_0<R_i$, the same condition as (15) holds, therefore

$$B_{\theta 1}^{r_0}=-\frac{1}{r_0}A_{z1}^{r_0}. \quad (20)$$

The transfer relations evaluated at R_i and r_0 gives us

$$\begin{bmatrix}B_{\theta 1}^d\\ B_{\theta 1}^{r_0}\end{bmatrix}=\begin{bmatrix}\frac{R_i^2+r_0^2}{R_i\left(r_0^2-R_i^2\right)} & \frac{2r_0}{R_i^2-r_0^2}\\ \frac{2R_i}{r_0^2-R_i^2} & \frac{R_i^2+r_0^2}{r_0\left(R_i^2-r_0^2\right)}\end{bmatrix}\begin{bmatrix}A_{z1}^d\\ A_{z1}^{r_0}\end{bmatrix}. \quad (21)$$

Using (19–21), we obtain

$$B_{\theta 1}^{r_0}=B_{\theta 1}^d=-B_{re}\ln\rho \quad (22)$$

$$A_{z1}^{r_0}=\frac{r_0}{R_i}A_{z1}^d=r_0B_{re}\ln\rho. \quad (23)$$

To determine $B_{r1}^{r_0}$, from (11), (12), and (23), we have

$$B_{r1}^{r_0} = \frac{1}{r_0} A_{z1}^{r_0} = B_{re} \ln \rho. \tag{24}$$

Now the magnetic flux density at the point of interest, (r_0, θ_0), can be found using (12), (22), and (24) as

$$\boldsymbol{B}_1^{r_0} = B_{re} \ln \rho \left[\cos\left(\theta_0\right) \boldsymbol{i}_r - \sin\left(\theta_0\right) \boldsymbol{i}_\theta\right] = B_{re} \ln \rho \, \boldsymbol{i}_x. \tag{25}$$

B. Magnetic Design for the HTM

In practice, a Halbach cylinder with a finite length must be constructed from PM bars arranged around a circumference to resemble the cylinder's structure and to approximate the magnetic field of the ideal cylinder with the superimposition of the fields generated by the individual magnets. This unavoidable segmentation causes three major issues. First, the adjacent magnets of a segmented Halbach cylinder strongly repulse each other, making it challenging for the design and assembly of the cylinder to rigidly hold the magnets. Second, if arc-shaped PMs are not used, the segmentation introduces air gaps and/or geometrical errors (due to a square or trapezoidal cross section instead of an arc-shaped one) that alter the resultant magnetic field from the desired field. Third, the limited availability of the NdFeB PMs' sizes and shapes with desired magnetization orientations (as the trapezoidal ones in [20], for instance) can be a hurdle for one to realize a motor design at a certain scale. Arc- and wedge-shaped PMs can be found at a few sizes to form a PM cylinder [21]–[23]. However, in most cases, the magnets with the azimuthal magnetization direction (required for a Halbach array) are lacking. In some rare cases, full Halbach rings can also be constructed at a few sizes but are about an order of magnitude more costly compared to the square magnets with the same total volume [24].

Square-cross-sectional PMs are among the most commercially available magnets at any desirable range of dimensions and magnetic remanence. The advantage of using square magnets is that there is no need for a different magnetization in a PM for the azimuthal direction. Only one type of magnet can be rotated and placed at any desirable orientation in a Halbach assembly, as shown in Fig. 2. If the magnetic flux density generated by the segmented Halbach cylinder that uses a certain number of the same square magnets is verified to be within an allowable proximity of the theoretical field generated by the ideal cylinder, the utilization of that segmented Halbach cylinder in a Lontentz-force motor becomes feasible. We have verified this for a Halbach cylinder with two poles formed by twenty NdFeB magnets. This was done by comparing the analytical-calculation result of the ideal Halbach cylinder's flux density as in Section II-A with those of finite-element analysis (FEA) and actual measurements [18]. The magnetic flux densities from the FEA and the experimental results are within 3% of that from the analytical solution.

From the above analysis, we come up with an outer-rotor motor design using a Halbach cylinder formed by 20 square-cross-sectional magnets. The hollow cylinder generates a constant magnetic field in its interior. To take the advantage of this constant magnetic field, we use four planar coils grouped into two phases with a 90° phase difference. By energizing these two winding phases using two sine-wave currents with the same phase difference of 90°, a constant torque proportional to the current amplitude can be generated at any angular position of the rotor. Other advantages of this design include following:

1) the ease of fabricating the stator and cylinder;
2) simple torque computation;
3) a linear torque model.

With the uneven air gaps between the magnets (introduced by replacing the ideal cylinder with the segmented one using square magnets), the change in the magnetic field is still negligible (within 3%) compared to that of the ideal case, which cannot be perfectly implemented because the arc magnets have their inherent errors from the magnetizing process.

Compared to the limited-angular-range actuator in [9], our HTM has four planar Lorentz coils instead of one. With a uniform magnetic field generated in the interior of a Halbach cylinder, theoretically, two coils placed at a 90° phase difference are sufficient to make full rotations of 360°. However, with two coils where each coil is symmetric about the motor's central axis, one coil must be shorter and placed in the interior of the other so that their short sides (not effective for force generation) do not interfere. This makes the entire motor structure significantly longer than the length of the coil sides that are effective for force generation. Therefore, we designed a structure with four rectangular coils symmetrically arranged as a cross configuration in the stator as shown in Fig. 4. Two opposite coils (top and bottom) are connected to form phase A, and the other coils (left and right) form phase B. With this, by flowing two sine-wave currents with the same amplitude and a 90° phase difference into the motor phases, a constant torque can be generated at any angular position.

Compared to conventional direct-current and stepper motors, which only have preferred positions aligned with the pole or slot locations, our motor can stop at any angular position. It can generate a continuous torque at any angular position. Theoretically, its positioning resolution is only limited by the sensing resolution of the rotor position and the resolution of the digital-analog-conversion (DAC) circuits that help provide the coil currents.

C. Mechanical Design and Assembly

At the center of the motor's cross-sectional view and stator's 3D model shown in Figs. 2, 4, and 5 is the coil mount (that houses four Lorentz coils in a cross configuration) where the two ball bearings are assembled at the two ends. This part is designed so that it is 3D-printable and on it the assembly of the coils and bearings are straightforward. In the same part, there are slots to mount the Hall-effect sensors for angular position sensing via the magnetic-field measurements. Fig. 4(b) shows the design of the full stator assembly with the four coils, the two ball bearings, and the stator coil housing as seen in Fig. 4(a). The hole at the center of the part on the left side is for the coils' end turns and sensors' wires to exit. Fig. 5 depicts the relative positions between the stator coils and the moving magnets. The magnet cylinder is fabricated by 3D printing the magnet housing

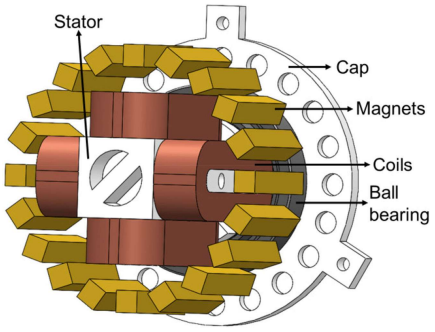

Fig. 5. 3-D rendering of the motor's stator and the magnets.

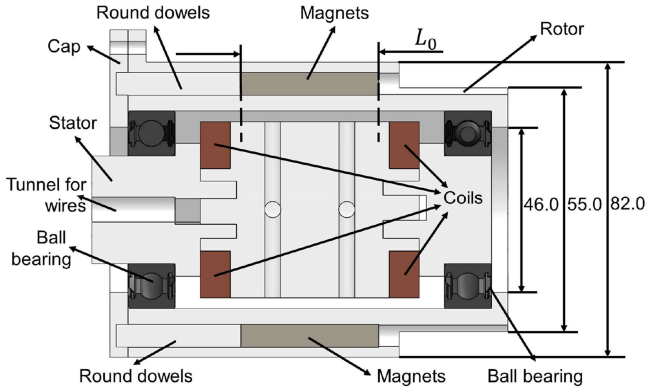

Fig. 6. Section view of the motor along its axis (length unit: mm).

as in Fig. 2 and inserting the magnets one by one along the axial direction of the housing.

The PMs' cross-sectional area is 6.35 × 6.35 mm and their length is 38.1 mm, which is the same as the effective length for force generation of the four planar Lorentz coils of the design. The outer part as in Figs. 2 and 6 is the housing that contains 20 magnets used to form the Halbach cylinder of our design. This 3D-printed magnet housing has the advantages of low cost, light weight that helps reducing the inertia for the rotor, and the capability of housing the magnets which can be oriented at any angle. The outer rings of the ball bearings are assembled at the two ends of this magnet housing. The material used to 3D-print the stator and rotor housings is ABS plastic.

In this design, each coil contains seven layers of American wire gauge #22 copper wires with 15 turns per layer. The average distance between each layer is around 0.7 mm which is larger than the diameter of the wires due to the bonding layer covering each wire turn. The coils have a fill factor of 53%. The locations marked as "coils" in Fig. 6 are the coils' end turns (or shorter sides), while the longer sides which are effective for force generation are along the motor axis and hidden from this section view. The dimensions of the motor structure are given in Fig. 6. The outside diameter of the Halbach cylinder is 76.4 mm. The overall diameter of the motor is 82.0 mm and its total length is 110.0 mm. The motor's total mass is 1.07 kg and the moment of inertial of its rotor is 5.5×10^{-4} kg.m^2.

The two Hall-effect sensors (to measure the magnetic flux density, from which the rotor position is calculated in real time) are placed on the small flat surfaces at the tips of the cross-shaped coil-mount structure shown in Figs. 2 and 4(a). These Hall-effect sensors are placed at a distance of 14.5 mm from the motor axis. We have verified that, at this radius, the magnetic flux density generated by our Halbach cylinder is a uniform field [18]. Therefore, the Hall-effect sensors should detect a sinusoidal magnetic flux density with respect to time if the rotor rotates at a constant speed. The period of 2π of this sinusoidal profile corresponds to one full rotation of the rotor. Along with the Hall-effect sensors we use temperature sensors, which are placed on the coils' surfaces, to monitor the temperature of the coils for a safety purpose and to update the temperature-dependent sensitivity of the Hall-effect sensors.

D. Electronic Design and Hardware Implementation

The magnetic flux density generated by the Halbach cylinder at the locations of the Hall-effect sensors is 157 mT [18]. The Hall-effect sensor selected for this range is DRV5055A4. It can detect the range of ±169 mT at a 5-V output voltage with a bandwidth of 20 kHz [25]. The relation between the output voltage V_{out} and the magnetic flux density B is as follows [25]:

$$V_{\text{out}} = V_Q + B \cdot \text{Sensitivity}\,(25\,^\circ\text{C}) \cdot \left[1 + S_{TC}\,(T_A - 25\,^\circ\text{C})\right]. \tag{26}$$

Here $V_Q = 2.5$ V, which is half V_{CC}, and T_A is the ambient temperature, which is measured by a temperature sensor at each coil phase. The sensors' sensitivity at 25 °C is 12.5 mV/mT, and S_{TC} is 0.0012/°C [25]. Thus, B is expressed as follows:

$$B = \frac{V_{\text{out}} - 2.5\text{V}}{\left[1 + 0.0012/^\circ\text{C} \cdot (T_A - 25\,^\circ\text{C})\right] 12.5\text{mV/mT}}. \tag{27}$$

The temperature sensors are TMP36, which has sensing range of −40 to 125 °C and provides a 750-mV output at 25 °C with the scaling factor of 10 mV/°C [26]. The relation between the temperature T and the output voltage V_T is

$$T = V_T \cdot 0.1\,^\circ\text{C/mV} - 50\,^\circ\text{C}. \tag{28}$$

The magnetic-flux-density resolution of our measurement setup is calculated from the analog-to-digital-conversion resolution, voltage swing, and sensor sensitivity to be 0.39 mT at 25 °C and 0.36 mT at 80 °C, which is translated to the theoretical angular position resolution of approximately 0.16°.

Our simulation and test results show that the maximum magnetic flux density on the Hall-effect sensors that the coils generate with the current amplitude at 4 A is approximately 10 mT. This would cause an angular error of 4° in the position measurement. However, the max current amplitude of 4 A is only needed when the motor operates at 270 r/min (1620 °/s). When precision positioning at a lower speed as presented in Section III-C is performed, the current amplitude is significantly smaller, and, therefore, the sensor readout affected by the stator's magnetic field is negligible.

Two digital-to-analog converters, MCP4725, are used to convert the control signals to the analog voltages to drive the power amplifiers that provide the currents to the two-phase armature coils [27]. The MCP4725 units are interfaced with the microcontroller through the I2C protocol.

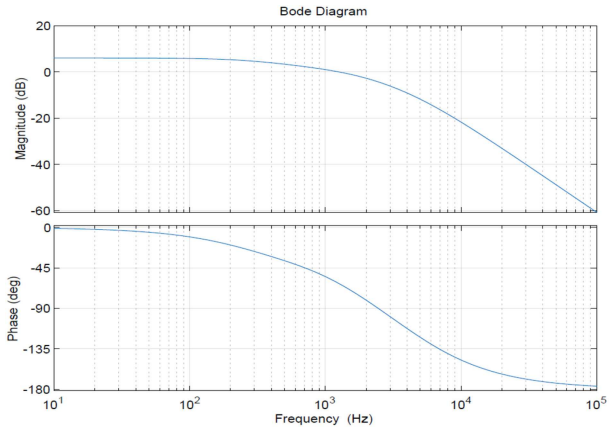

Fig. 7. Bode plot of the transconductance power amplifier circuit.

For the power-amplifier circuits, two PA12A power operational amplifiers with excellent linearity and thermal stability are used [28]. The circuit diagram can be found in our previous work [29]. For this HTM, two channels are used, and each amplifier energizes one phase of the two-phase motor. The transfer function of the circuit between voltage input $V_{\text{in}}(s)$ and the current output $I_a(s)$ is given [29] as (29) shown at the bottom of this page.

Each phase with two coils has an inductance of $L_a = 152\ \mu$H and a resistance of $R_a = 1.5\ \Omega$. All capacitors are 10 nF. Resistors R_1–R_9 are 10 kΩ and R_{10} is 1.0 Ω with 10 W. The capacitor C_3 and resistor R_6 form a PI controller to eliminate the steady-state error of the current output.

Fig. 7 shows the Bode plot of the amplifier circuit with the load of one motor phase, R_a and L_a. The motor's effective closed-loop control bandwidth is below 10 Hz, and the amplifier's phase lag is less than 1.2° at 10 Hz. Therefore, the delay in the dynamics of the transconductance amplifiers is negligible. The circuits have the capability to generate accurate currents within the range of –4.0 to 4.0 A with a resolution of 2.44 mA. Because the transconductance amplifier circuit generates the current output with an onboard PI controller that eliminates the current error, the back emf generated by the motor can also be neglected in the control system.

III. Dynamics and Control

A. Motor Dynamic Analysis

Fig. 8 is the sensing and control-hardware diagram of the motor. Fig. 9(a) and (b) are the detailed and simplified diagrams of the motor's closed-loop control system. The angle between the magnetic axis of phase A and the magnetic axis of the Halbach magnet cylinder, as depicted in Fig. 2, is ψ.

Under the assumption that the system has a damping torque of τ_c, a damping coefficient of c, and a Coulomb friction torque τ_f with the coefficient K_f, the motor's equation of motion can be derived as in (30), (31), where J_m is the moment of inertia of the rotor.

$$J_m\ddot{\psi} + \tau_c + \tau_f = \tau_m \tag{30}$$

$$J_m\ddot{\psi} + c\dot{\psi} + K_f \text{sgn}\left(\dot{\psi}\right) = \phi_m I(t). \tag{31}$$

With a constant phase-current input in steady state at a certain speed, (31) becomes

$$I = \frac{c}{\phi_m}\dot{\psi} + \frac{K_f}{\phi_m} \tag{32}$$

where ϕ_m is the maximum net magnetic flux penetrating the cross-sectional area of coils or the torque constant [18].

The angular velocity of the motor $\dot{\psi}$ is measured with various current amplitudes to identify the damping torque τ_c and the Coulomb friction torque τ_f. The experimental results are given in Fig. 10, and $\phi_m = 1.43 \times 10^{-2}$ Wb. We have $c = 1.23 \times 10^{-3}$ N · m·s and $K_f = 2.05 \times 10^{-2}$ N · m. The R^2 value of this linear fit is 0.9965.

B. Controller Design

There are advanced robust control methods for electric motors as presented in [30], [31]. However, these methods are not suitable for embedded control platforms with limited computational resources. In our case, with the dynamic model and all parameter values identified, a PI controller is designed and tested. The reason we choose a PI control structure is that it has been demonstrated to produce satisfying control performance with Lorentz-force motors in precision motion control [11], [29]. In addition, our target is to develop a simple control method that can be effectively implemented in most embedded-control platforms.

In Fig. 9, our controller and plant are $C(s) = K_P + K_I/s$ and $G(s) = \phi_m/(J_m s^2 + cs)$, respectively. The Coulomb friction is not included in this linear transfer-function model.

The closed-loop transfer function of the system in the continuous domain and the system error $\Psi_e(s)$ are as follows:

$$\frac{\Psi(s)}{\Psi_r(s)} = \frac{G(s)C(s)}{1 + G(s)C(s)} = \frac{\phi_m K_P s + \phi_m K_I}{J_m s^3 + cs^2 + \phi_m K_P s + \phi_m K_I} \tag{33}$$

$$\Psi_e(s) = \frac{1}{1 + G(s)C(s)}\Psi_r(s) = \frac{J_m s^3 + cs^2}{J_m s^3 + cs^2 + \phi_m K_p s + \phi_m K_I}\Psi_r(s). \tag{34}$$

This third-order transfer function of the system can be approximated with a second-order dominant system having the characteristic polynomial of $(s+\alpha)(s^2 + 2\zeta\omega_n s + \omega_n^2)$, where ζ is the closed-loop damping ratio and ω_n is the undamped closed-loop natural frequency. Compared to the denominator in (33), the relations between the poles and the control parameters can be derived as

$$\alpha + 2\zeta\omega_n = c/J_m \tag{35}$$

$$\frac{I_a(s)}{V_{\text{in}}(s)} = \frac{R_3 \cdot R_7 \cdot (R_9 + R_8)(R_6 C_3 s + 1)}{R_1 R_5 \left[\frac{R_{10}}{2}(R_9 + R_8)(R_6 C_3 s + 1) + R_9 R_7 C_3 \left(L_a s + R_a + \frac{R_{10}}{2}\right) s\right](R_3 C_2 s + 1)}. \tag{29}$$

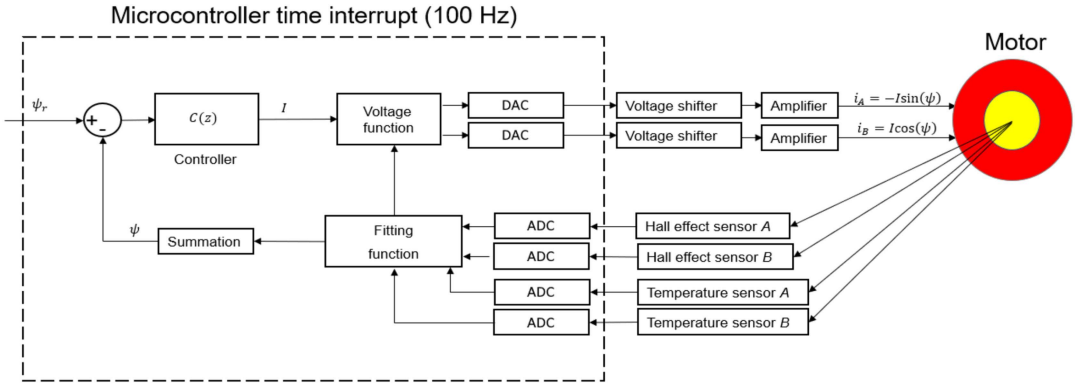

Fig. 8. Hardware block diagram of the HTM in the control loop.

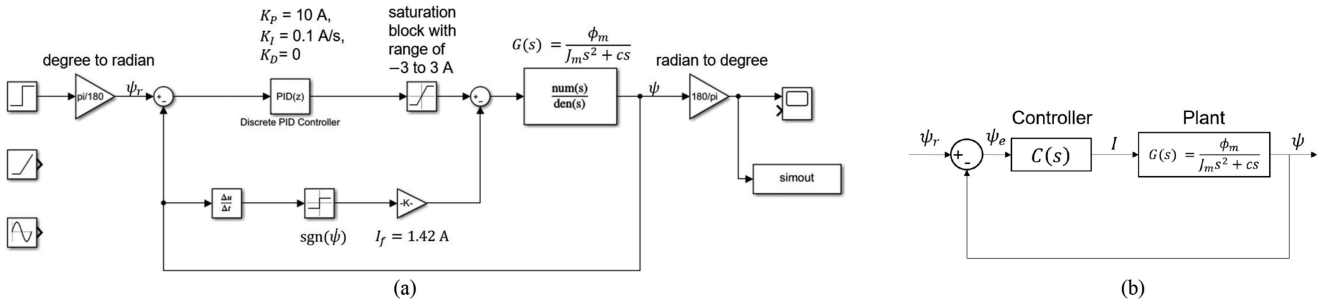

Fig. 9. (a) Detailed block diagram for the control simulation and (b) the simplified diagram of the HTM's closed-loop control system.

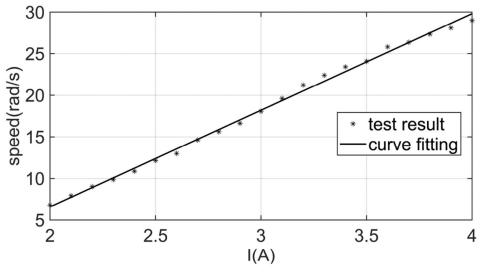

Fig. 10. Measured speeds with a set of current–amplitude inputs.

$$\omega_n^2 + 2\zeta\omega_n\alpha = \phi_m\, K_P/J_m \tag{36}$$

$$\alpha\,\omega_n^2 = \phi_m\, K_I/J_m. \tag{37}$$

Due to the Coulomb friction of the motor that is not included in the linear model represented by the transfer function, the closed-loop system has a short rising time of $t_r = 0.12$ s and only a small added damping of $\zeta = 0.06$. The nature frequency is $\omega_n \cong 1.8/t_r = 15$ rad/s. The proportional gain of the controller is $K_P = (J_m/\phi)(\omega_n^2 + 2\zeta\omega_n\alpha) \cong 10$ A/rad and the integral gain is $K_I = \alpha\omega_n^2 J_m/\phi_m \cong 0.1$ A/rad.s. The digital controller converted using the zero-order-hold equivalence is

$$C(z) = \frac{I(z)}{\Psi_e(z)} = K_p + \frac{T_s K_I z^{-1}}{1 - z^{-1}} \tag{38}$$

with the sampling period $T_s = 0.01$ s. The closed-loop system without the Coulomb friction has a 4-Hz bandwidth, and the controller with time interrupt is set at 100 Hz. In the real-time control program, the difference equation for the control current at the kth iteration is

$$i[k] = 10e[k] - 10e[k-1] + i[k-1] \tag{39}$$

where $e[k] = \psi_r - \psi[k]$.

In the real-time implementation, a fitting function repeatedly sends the position data which ranges from 0° to 360° to the DAC-voltage-calculation function. As shown in Fig. 8, this function receives the control input from the main controller to calculate the DAC voltages to be sent to the current amplifiers in real time. The summation block in Fig. 8 gives the accumulation of the angular-position data to the controller.

C. Experimental Results

In this article, the HTM is tested with the step inputs at various positions, speed inputs, and sinusoidal inputs. The theoretical angular resolution of our measurement setup is 0.16°. The controller can perform angular motions with a minimum step of 0.32°, for which the consecutive step responses are shown in Fig. 11. With a sine-wave reference at 1 Hz, the response is provided in Fig. 12. In this case, we see a certain amount of phase lag in the response because the designed closed-loop control bandwidth is only 4 Hz.

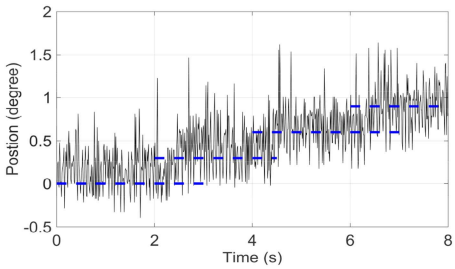

Fig. 11. Experimental result showing consecutive steps of 0.32°.

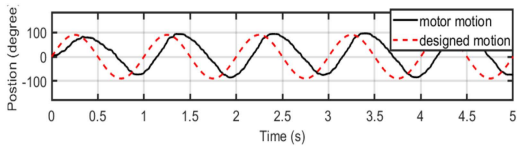

Fig. 12. Response to a 1-Hz sine-wave reference.

The experimental results to be compared with the simulation described in Fig. 9(a) are given in Fig. 13 to show the motor's control performance. Here, the dashed lines represent the simulation results by Matlab Simulink. In Fig. 13(a), the motion of the motor has a significant rising time with some overshoot as predicted in the controller design. There are some transient ridges from the nonlinear behavior caused by the fitting function with a linear fit to the sinusoidal magnetic flux density. The position error is within $\pm 0.64°$. Fig. 13(b) shows that the motor tracks the ramp input well in steady state with the reference speed of 83 r/min. When $t < 1.5$ s, there is a hunting transient shown in the figure, which is consistent with the simulation result. Fig. 13(c) and (d) shows that the system effectively tracks the sinusoidal references. The motor tracks the reference well within 1.9 s in Fig. 13(c) and 3.7 s in Fig. 13(d), and closely follows the reference since then. The larger the amplitude is, the longer it takes for the motor to reach and closely follow the reference. With this, our HTM is proved feasible for the precision rotary position-control applications.

IV. Conclusion

This article presents the design and control of a novel cylindrical Halbach-array-based two-phase motor. This is an external-rotor design with the rotor being a two-pole Halbach cylinder formed by 20 NdFeB magnets with a square cross section. The Halbach cylinder generates a uniform magnetic field within its inner diameter where the four stationary Lorentz coils are placed. The 3D-printed coil and magnet housings are low cost and easy to fabricate and assemble. The structure can easily be scaled to a variety of sizes thanks to the prevalent availability of square-cross-section magnets and the 3D-printed magnet housing being able to house the magnets oriented at any angle. The uniform magnetic field and the two-phase Lorentz coils allow for a simple linear system model to be identified from experiments. For feedback control, the rotor position is sensed by Hall-effect sensors and, therefore, no external encoder is needed. With a PI controller designed and implemented, the motor achieved an angular resolution of 0.32°, which is twice as large as the theoretical resolution of the measurement setup. The motor can track the sinusoidal reference at 0.2 Hz well within 0.64°. This motor design can, therefore, be highly applicable in a variety of precision applications including radar and lidar position control.

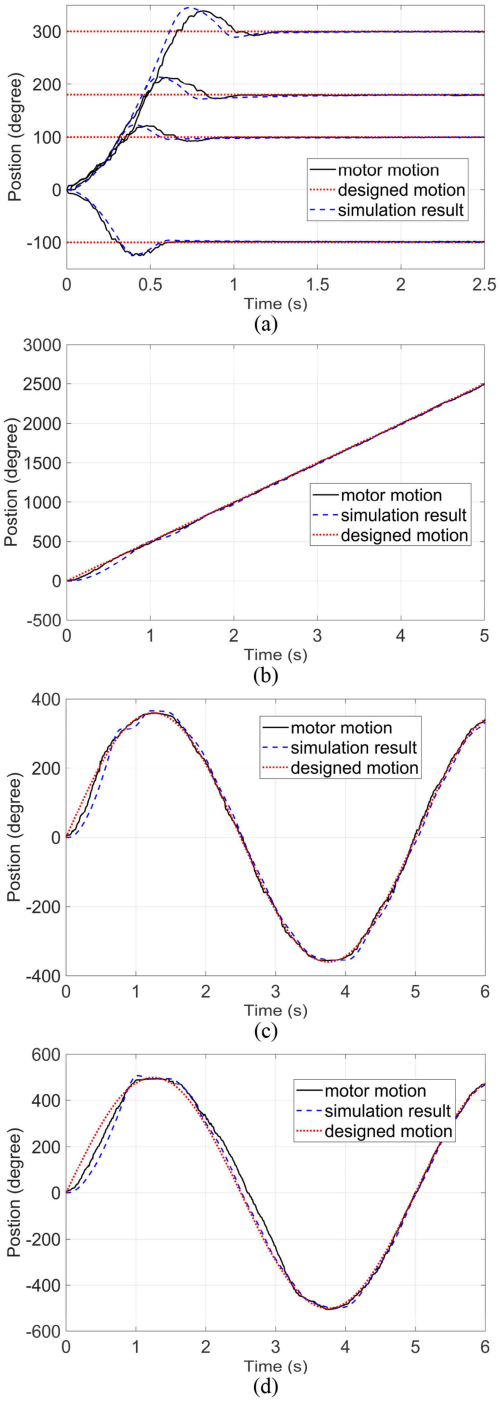

Fig. 13. (a) Step responses ($\pm 100°$, 180°, 300°), (b) ramp response (at 500 °/s), (c) sinusoidal reference response with the magnitude of 360° and period of 5 s, and (d) sinusoidal reference response with the magnitude of 500° and period of 5 s.

REFERENCES

[1] D. S. Hall, "High definition Lidar system," U.S. Patent 2011/0216304 A1, Aug., 2011.

[2] Renishaw Incorporation, "Optical encoders and LiDAR scanning," Accessed: Feb. 2020. [Online]. Available: www.renishaw.com/en/optical-encoders-and-lidar-scanning--39244

[3] K. Halbach, "Design of permanent multipole magnets with oriented rare earth cobalt material," *Nucl. Instruments Methods*, vol. 169, no. 1, pp. 1–10, Feb. 1980.

[4] K. Atallah and D. Howe, "The application of Halbach cylinders to brushless AC servo motors," *IEEE Trans. Magn.*, vol. 34, no. 4, pp. 2060–2062, Jul. 1998.

[5] W.-J. Kim, D. L. Trumper, and J. H. Lang, "Modeling and vector control of planar magnetic levitator," *IEEE Trans. Ind. Appl.*, vol. 34, no. 6, pp. 1254–1262, Nov./Dec. 1998.

[6] Z. Q. Zhu, Z. P. Xia, and D. Howe, "Comparison of Halbach magnetized brushless machines based on discrete magnet segments or a single ring magnet," *IEEE Trans. Magn.*, vol. 38, no. 5, pp. 2997–2999, Sep. 2002.

[7] T. Hu and W.-J. Kim, "Extended range six-DOF high-precision positioner for wafer processing," *IEEE/ASME Trans. Mechatronics*, vol. 11, no. 6, pp. 682–689, Dec. 2006.

[8] Y. Shen, G. Y. Liu, Z. P. Xia, and Z. Q. Zhu, "Determination of maximum electromagnetic torque in PM brushless machines having two-segment Halbach array," *IEEE Trans. Ind. Electron.*, vol. 61, no. 2, pp. 718–729, Feb. 2014.

[9] S.-L. Chen *et al.*, "Toward comprehensive modeling and large angle tracking control of a limited angle torque actuator with cylindrical Halbach," *IEEE/ASME Trans. Mechatronics*, vol. 21, no. 1, pp. 431–442, Feb. 2016.

[10] M. Dyck, X. Lu, and Y. Altintas, "Magnetically levitated rotary table with six degrees of freedom," *IEEE/ASME Trans. Mechatronics*, vol. 22, no. 1, pp. 530–540, Feb. 2017.

[11] V. H. Nguyen and W.-J. Kim, "Two-phase Lorentz coils and linear Halbach array for multiaxis precision-positioning stages with magnetic levitation," *IEEE/ASME Trans. Mechatronics*, vol. 22, no. 6, pp. 2662–2672, Dec. 2017.

[12] P. R. Eckert, E. C. Goltz, and A. F. F. Filho, "Influence of segmentation of ring-shaped NdFeB magnets with parallel magnetization on cylindrical actuators," *Sensors*, vol. 14, no. 7, pp. 13070–13087, Jul. 2014.

[13] D. Trbojevic, "Halbach magnets for CBETA," Brookhaven National Laboratory, Upton, NY, USA, Tech. Rep. BNL-114540-2017-IR, Jan. 2017.

[14] H. Witte, J. S. Berg, and B. Parker, "Halbach magnets for CBETA and eRHIC," in *Proc. 8th Int. Particle Accel. Conf.*, 2017, pp. 4814–4816.

[15] T. R. N. Mhíocháin, D. Weaire, S. M. McMurry, and J. M. D. Coey, "Analysis of torque in nested magnetic cylinders," *J. Appl. Phys.*, vol. 86, no. 11, pp. 6412–6424, Nov. 1999.

[16] Z. H. Ren, W. C. Mu, and S. Y. Huang, "Design and optimization of a ring-pair permanent magnet array for head imaging in a low-field portable MRI system," *IEEE Trans. Magn.*, vol. 55, no. 1, pp. 1–8, Jan. 2019.

[17] A. Insinga, C. Bahl, R. Bjørk, and A. Smith, "Performance of Halbach magnet arrays with finite coercivity," *J. Magnetism Magn. Mater.*, vol. 407, pp. 369–376, Jun. 2016.

[18] Y. Wei, "Analysis, design, and control of a novel Halbach-array-based two-phase motor," M.S. thesis, Dept. Mech. Eng., Texas A&M Univ., College Station, TX, USA, Dec. 2020.

[19] J. R. Melcher, "Electrodynamic laws, approximations and relations," in *Continuum Electromechanics*. Cambridge, MA, USA: MIT Press, 1981.

[20] O. Winter, C. Kral, and E. Schmidt, "Design study of magnet shapes for axial Halbach arrays using 3D finite element analyses," in *Proc. 20th Int. Conf. Elect. Mach.*, 2012, pp. 2660–2665.

[21] SuperMagnetMan, "Arcs," Accessed: Feb. 2020. [Online]. Available: https://supermagnetman.com/collections/neo-arcs

[22] Applied Magnets, "Neodymium arc & wedge rare earth magnets," Accessed: Feb. 2020. [Online]. Available: https://appliedmagnets.com/neodymium-arc-wedge-rare-earth-magnets-c-1_16.html

[23] CMS Magnetics, "Neodymium magnets," Accessed: Feb. 2020. [Online]. Available: www.magnet4sale.com/neodymium-magnets

[24] SuperMagnetMan, "Halbach assemblies," Accessed: Feb. 2020. [Online]. Available: https://supermagnetman.com/collections

[25] Texas Instruments, "DRV5055 ratiometric linear hall-effect sensor," Accessed: Dec. 2020. [Online]. Available: https://www.ti.com/lit/ds/symlink/drv5055.pdf?ts=1626039076119&ref_url=https%253A%252F%252Fwww.google.com%252F

[26] Analog Devices, "Low voltage temperature sensors TMP35/TMP36/TMP37," D00337-0-5/15(H) datasheet, May 2015.

[27] Microchip, "MCP4725 12-Bit digital-to-analog converter with EEPROM memory in SOT-23-6," DS22039D datasheet, Mar. 2009.

[28] A. Microtechnology, "PA12A power operational amplifier," PA12UREVV datasheet, Oct. 2012.

[29] V. H. Nguyen, "Universal framework for linear motors and multi-axis stages with magnetic levitation," Ph.D. dissertation, Dept. Mech. Eng., Texas A&M Univ., College Station, TX, USA, Nov. 2015.

[30] M. Preindl, "Robust control invariant sets and Lyapunov-based MPC for IPM synchronous motor drives," *IEEE Trans. Ind. Electron.*, vol. 63, no. 6, pp. 3925–3933, Jun. 2016.

[31] F. F. M. El-Sousy, M. M. Amin, and O. A. Mohammed, "Robust optimal control of high-speed permanent-magnet synchronous motor drives via self-constructing fuzzy wavelet neural network," *IEEE Trans. Ind. Appl.*, vol. 57, no. 1, pp. 999–1013, Jan./Feb. 2021.

Yuan Wei received the B.Eng. degree in mechanical engineering from Shanghai Jiao Tong University, Shanghai, China, in 2018 and the M.S degree in mechanical engineering from Texas A&M University, College Station, TX, USA, in 2020, where he is currently working toward a Ph.D. degree.

His research interests include robotic mechanism design, design and analysis of permanent magnet motors, and real-time control of mechatronic systems.

Vu Huy Nguyen (Member, IEEE) received the B.S. degree from the Hanoi University of Technology, Hanoi, Vietnam, in 2005, and the M.S. and Ph.D. degrees from Texas A&M University, College Station, TX, USA, in 2011 and 2015, respectively, all in mechanical engineering.

Since 2019, he has been with the Lawrence Berkeley National Laboratory, Berkeley, CA, USA. His research interests include the explorations of new approaches in design, modeling, and control to realize ultraprecision opto-mechanical systems.

Won-jong Kim (Senior Member, IEEE) received the B.S. (*summa cum laude*) and M.S. degrees from Seoul National University, Seoul, Korea, in 1989 and 1991, respectively, both in control and instrumentation engineering, and the Ph.D. degree in electrical engineering and computer science from the Massachusetts Institute of Technology, Cambridge, MA, USA, in 1997.

Since 2000, he has been with the Department of Mechanical Engineering, Texas A&M University, College Station, where currently he is an Associate Professor and was the inaugural Holder of the Dietz Career Development Professorship II in 2007–2010. He is the holder of three U.S. patents on precision positioning systems. His current research interests include the analysis, design, and real-time control of mechatronic systems, networked control systems, and nanoscale engineering and technology.

Prof. Kim is Fellow of ASME and a Member of Pi Tau Sigma. He is also the Editor of *International Journal of Control, Automation, and Systems*, and is or was Technical Editor of IEEE/ASME TRANSACTIONS ON MECHATRONICS, *ASME Journal of Dynamic Systems, Measurement and Control,* and *Asian Journal of Control*.